Retrieval of Raindrop Size Distribution from Simulated Dual-Frequency Radar Measurements

S. JOSEPH MUNCHAK

Department of Meteorology, The Pennsylvania State University, University Park, Pennsylvania

ALI TOKAY

Joint Center for Earth Systems Technology, University of Maryland, Baltimore County, Baltimore, and NASA Goddard Space Flight Center, Greenbelt, Maryland

(Manuscript received 28 June 2006, in final form 21 February 2007)

ABSTRACT

Observations of raindrop size distributions (DSDs) have validated the use of three-parameter distribution functions in representing the observed spectra. However, dual-frequency radar measurements are limited to retrieving two independent parameters of the DSD, thus requiring a constraint on a three-parameter distribution. In this study, disdrometer observations from a variety of climate regions are employed to develop constraints on the gamma distribution that are optimized for dual-frequency radar rainfall retrievals. These observations are composited by reflectivity, and then gamma parameters are fit to the composites. The results show considerable variability in shape parameter between regions and within a region at different reflectivities. Most notable is that oceanic regions exhibit maxima in shape parameter at 13.6-GHz reflectivities between 40 and 50 dBZ, in contrast to continental regions. The shape parameter and slope parameter of all composite DSDs are poorly correlated. Thus, constraints of a constant shape parameter or shape parameter–slope parameter relationship are inadequate to represent the observed variability. However, the shape and slope parameters are highly correlated at a given reflectivity. Constraints of a fixed shape parameter and relationships between a shape parameter m and slope parameter Λ, both of which are given as functions of 13.6-GHz reflectivity, are applied to retrieve rain rate, liquid water content, and mean mass diameter from the composites. The m–Λ relationships perform best at high reflectivity (dB$Z_{13.6} > 35$), whereas the fixed shape parameter generally results in lower error at medium and low reflectivities (dB$Z_{13.6} < 35$). All calculations have been made under the assumption that the reflectivity measurements have been corrected for attenuation.

1. Introduction

Knowledge of the raindrop size distribution (DSD) is of fundamental interest to the atmospheric sciences community in relation to modeling studies and radar-rainfall estimation. Modelers seek realistic DSD representation in microphysical parameterizations, where DSD is critical for latent heating, radiative transfer, and quantitative precipitation estimation. Radar meteorologists require knowledge of the DSD to relate radar reflectivity Z to rainfall rate R. Because there is not a one-to-one correspondence between the two quantities, a wide range of Z–R relations have appeared in the literature (Battan 1973). For example, different relations are often prescribed either for different rainfall processes, for example, stratiform versus convective (Tokay and Short 1996), or in different climate regimes, for example, continental versus maritime (Bringi et al. 2003), owing to the different microphysical processes that contribute to DSD evolution.

Most of the earth's rain falls over the oceans, especially in the tropics. For studies of the global hydrologic cycle, it is therefore critical that rainfall measurements be made here. Since its launch in November 1997, the National Aeronautics and Space Administration (NASA) Tropical Rainfall Measuring Mission (TRMM) satellite estimates rainfall at tropical and subtropical latitudes, employing a 13.8-GHz precipitation radar (PR) and the TRMM Microwave Imager (TMI;

Corresponding author address: Ali Tokay, NASA Goddard Space Flight Center, Code 613.1, Greenbelt, MD 20771.
E-mail: tokay@radar.gsfc.nasa.gov

DOI: 10.1175/2007JAMC1524.1

© 2008 American Meteorological Society

Kummerow et al. 1998). However, because the PR operates at a single frequency, it is subject to errors resulting from the regional variability of DSD (Berg et al. 2006). The upcoming Global Precipitation Measurement (GPM) mission will improve upon TRMM by employing a dual-frequency precipitation radar (Iguchi et al. 2003). The dual-frequency radar offers an additional measurement with the potential to reduce the uncertainties in DSD estimation that are inherent with single-frequency radar. In addition, microwave radiometers on the core satellite and constellation satellites will provide a global precipitation measuring platform with high temporal frequency and spatial coverage.

The dual-frequency radar is one of several multiparameter radar technologies developed to estimate DSD more precisely. Other such technologies include polarimetric radar measurements (Bringi et al. 2002), vertically pointed radars (Williams 2002), and a microwave link (Rincon and Lang 2002). Of these, dual-frequency radar is the most suitable for satellite-based observations (Kuo et al. 2004). The choice of frequencies is subject to power and antenna size requirements as well as attenuation (Iguchi et al. 2003). The frequencies should also be sufficiently separated so that reflectivity measurements have different dependencies on the DSD (Meagher and Haddad 2006). In consideration of these requirements, Ku- (13.6 GHz) and Ka-band (35 GHz) frequencies have been designated for the GPM core satellite.

Previous studies involving dual-frequency radar have attempted to improve upon single-frequency Z–R relations through a variety of techniques. Eccles and Mueller (1971) employed 3- and 10-GHz frequencies to estimate liquid water content via differential attenuation, which is more closely related to rain rate than reflectivity. Goldhirsh and Katz (1974) advanced dual-frequency techniques by deriving two parameters of an exponential DSD function directly from the two radar measurements, although their method was constrained by the assumption of constant rain rate over a path. Meneghini et al. (1992) pioneered the use of downward-looking airborne dual-frequency measurements of reflectivity and attenuation to formulate the retrieval of DSD from spaceborne radar measurements. A crucial element of this study was the use of frequencies where non-Rayleigh scattering allowed the retrieval of DSD parameters from attenuation-corrected reflectivities.

In general, the availability of two independent reflectivity measurements allows for the retrieval of only two parameters describing the DSD. This naturally poses questions of how many parameters are sufficient to describe the range of DSDs observed in nature, and how to optimally model the DSD with only two independent parameters. These questions have been the subject of extensive study since DSD measurements have been available. Although there has been a recent study in Bayesian techniques where no a priori distribution is prescribed (Haddad et al. 2006), the three-parameter gamma distribution is mostly employed to retrieve the DSD from reflectivity and/or attenuation measurements. In this study we use a form of the gamma distribution expressed as

$$N(D) = N_0 D^m e^{-\Lambda D}, \tag{1}$$

where N_0 is the intercept parameter, Λ is the slope parameter, and m is the shape parameter. The exponential distribution is a special form of the gamma distribution for which the shape parameter is equal to zero. In an exponential distribution, the drop concentration per unit diameter $N(D)$ increases with decreasing diameter at a rate that is determined by the slope parameter. Marshall and Palmer (1948) introduced a special form of the exponential size distribution where N_0 is constant and Λ is a function of rain rate. Since their pioneering study, both surface and airborne measurements of the DSD have illustrated that the shape of the spectra deviates from the exponential distribution at small and large drop sizes. There is often some degree of curvature around a peak concentration near 1-mm diameter. The gamma distribution with a positive shape parameter may accurately represent this curvature as shown in Tokay and Short (1996).

When dual-frequency measurements are applied to the three-parameter gamma distribution, the lack of a third radar measurement introduces a challenge, and the number of independent parameters must be reduced. This reduction can be achieved either by assuming a value for one of the parameters, or by specifying relationships among some of the parameters. Indeed, there have been several studies in regard to empirical relations between the gamma parameters. Haddad et al. (1996) argued that the parameters given in Eq. (1) are not independent and introduced a new set of three parameters. Ulbrich (1983) illustrated that the shape and intercept parameters of the gamma distribution can be related. Zhang et al. (2001) and Brandes et al. (2003) introduced a constrained gamma distribution where a relationship between the slope and shape parameters was specified for use in polarimetric radar-rainfall retrievals. Although high correlation coefficients in these studies confirm the existence of such relations between the gamma parameters, the relations do not necessarily hold at all rain intensities and for all precipitation events.

In this study, we seek to develop optimal constraints on the three-parameter gamma distribution that allow for accurate DSD retrieval from dual-frequency reflectivity measurements. The framework for these measurements is described in section 2. In section 3, we describe the disdrometer datasets we employed to develop the constraints. The gamma parameters are fit to these measurements by a process described in section 4, and the results of this process are given in section 5. Relationships between the shape and slope parameter from these fits are derived in section 6 and evaluated in section 7. In the final section, we offer both a summary and concluding remarks.

2. Dual-frequency radar framework

Numerous algorithms (e.g., Meneghini et al. 1992; Mardiana et al. 2004; Iguchi 2005; Liao and Meneghini 2005) have been proposed to retrieve rainfall estimates from dual-frequency radar measurements. These algorithms aim to estimate the DSD at each range gate once the attenuation correction has been applied from previous range gates. In this study, we focus on DSD estimation and assume that the reflectivity measurements have been corrected for attenuation. These measurements of effective reflectivity Z_e are the integral product of backscattering cross section σ_b and the DSD. In general, Z_e is expressed as

$$Z_e = \frac{\lambda^4}{\pi^5|K|^2}\int_0^\infty N(D)\sigma_b(D, \lambda, T)\, dD, \tag{2}$$

where λ is the radar wavelength and $|K|^2$ is the dielectric factor, which is related to the complex index of refraction of the target and is sensitive to its temperature and the radar frequency. The backscattering cross section is a function of both the size and temperature of the drop and the radar frequency. The general solution to the backscattering cross section of a homogeneous sphere interacting with an electromagnetic plane wave is given by Mie theory. For drops much smaller than the radar wavelength, where the size parameter ($\pi D/\lambda$) is much less than 1, the backscattering cross section is well approximated by Rayleigh theory. At 13.6 and 35 GHz, however, the size parameter nears or exceeds 1 for drops larger than about 1 mm in diameter. At these drop sizes, the full Mie theory must be used to calculate the backscattering cross section at these two frequencies, which diverges from Rayleigh scattering (Fig. 1). As a result, the effective reflectivity of a DSD containing these drops is frequency dependent, a property that is exploited in the dual-frequency radar retrieval technique described in this study.

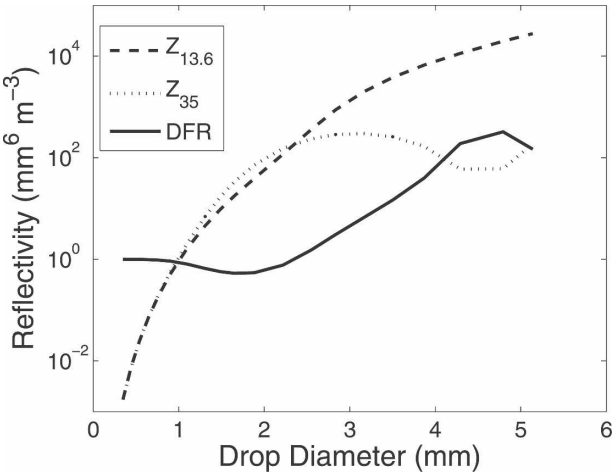

FIG. 1. Reflectivity and dual-frequency ratio of a single drop per cubic meter as a function of drop diameter for two different radar frequencies. The dielectric constant and backscattering cross sections were calculated for a temperature of 20°C.

The DSD dependence of Z_e can be shown by substituting the gamma distribution [Eq. (1)] into Eq. (2),

$$Z_e = \frac{\lambda^4}{\pi^5|K|^2}\int_{D_{\min}}^{D_{\max}} N_0 D^m e^{-\Lambda D}\sigma_b(D, \lambda, T)\, dD. \tag{3}$$

The difference between the reflectivity measurements is described by the dual-frequency ratio (DFR). This quantity is independent of the intercept parameter and is defined as

$$\mathrm{DFR} = \frac{Z_{13.6}}{Z_{35}} = \frac{\lambda_{13.6}^4|K_{35}|^2\int_{D_{\min}}^{D_{\max}}\sigma_{b,13.6}(D,T)D^m e^{-\Lambda D}\, dD}{\lambda_{35}^4|K_{13.6}|^2\int_{D_{\min}}^{D_{\max}}\sigma_{b,35}(D,T)D^m e^{-\Lambda D}\, dD}. \tag{4}$$

The DFR may be examined in shape parameter–slope parameter space (Fig. 2) where both gamma parameters are bound by the limits suggested by Tokay and Short (1996), who found that the slope parameter ranged between 1 and 20, while the shape parameter remained between −2 and 30. This upper limit on the shape parameter was lowered to 20 because subsequent research has shown that high shape parameters are a nonphysical product of biases in the method of moments (Smith and Kliche 2005). For a given DFR, an infinite number of solutions exists for the shape and slope parameters within these bounds. To reduce this set to a single solution, a constraint, such as a constant shape parameter (Liao and Meneghini 2005) or a rela-

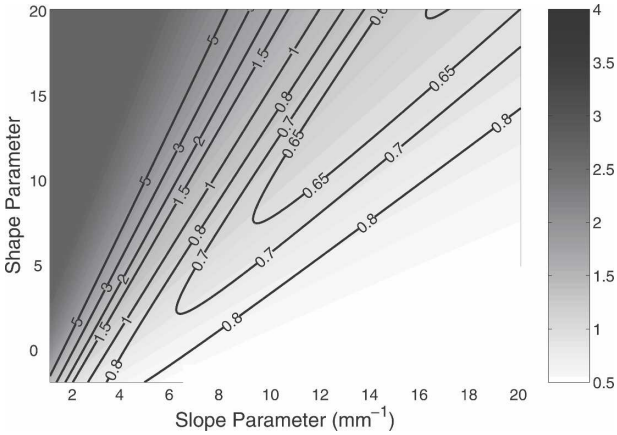

FIG. 2. Contour plot of DFR as a function of shape and slope parameter. Mean mass diameter, which is also a function of shape and slope parameter only, is illustrated by the shading.

tionship between the shape and slope parameters (Brandes et al. 2003), must be imposed, even though DSDs that deviate from these constraints could lead to retrieval errors.

Where the DFR is less than 1, the contours in Fig. 2 are hyperbolic curves. This characteristic represents a well-known ambiguity (Meagher and Haddad 2006) that is an obstacle for dual-frequency radar DSD retrievals. This ambiguity manifests itself in dual solutions for the slope parameter when a constraint of constant shape parameter is given. This is because the DFR of a single drop does not increase monotonically with drop size, but decreases from 1 at the limit of a small-drop diameter to a minimum of 0.53 at 1.8-mm diameter before increasing to values greater than 1 at larger drop diameters (Fig. 1). Thus, a DSD consisting of drops smaller than 1.8 mm may have the same DFR as a DSD including larger drops. This ambiguity can be reduced to some extent because the distribution containing only the small drops will, in all likelihood, have a lower reflectivity than the DSD with both small and large drops (Liao and Meneghini 2005), but then it is necessary to prescribe a threshold reflectivity at which the solutions switch over.

To further interpret Fig. 2, it is useful to draw upon relations between the gamma parameters and physical DSD parameters. The mean mass diameter (D_m) is the ratio of the fourth to third moments of the DSD and is related to the slope parameter of the gamma distribution (Ulbrich and Atlas 1998):

$$D_m = \frac{4 + m}{\Lambda}. \tag{5}$$

Many dual-frequency DSD retrieval studies (e.g., Meneghini et al. 1997; Kuo et al. 2004; Liao and Meneghini 2005) cite the median volume diameter D_0 instead, which is closely related to D_m:

$$D_0 = \frac{(11/3) + m}{4 + m} D_m. \tag{6}$$

The relationship between DFR and mean mass diameter is illustrated in Fig. 2. The D_m contours are nearly parallel to the DFR contours except at the apex of the DFR contours, indicating that DFR is a good proxy for D_m in most of the shape and slope parameter space. In general, mean mass diameter decreases with increasing slope parameter and decreasing shape parameter. This means that the smallest mean mass diameter is associated with a nearly exponential distribution with a steep slope. Conversely, the largest mean mass diameter is associated with a downward-curved spectrum where the slope is shallow, allowing the peak concentration to be at relatively large drop sizes.

When the peak concentration is at 1–2-mm diameter, the DFR is at a minimum because the lowest dual-frequency ratio is at these sizes (Fig. 1). The value of this minimum depends on the width of the distribution, which is related to the shape parameter. As shape parameter increases, the distribution becomes narrower and the minimum DFR decreases (Fig. 2). Therefore, the DFR provides a lower bound on the shape parameter, although this information is only useful when the limit is higher than a physically realistic lower bound of -2 (Ulbrich 1983). Likewise, the physically realistic upper bound of 20 on a shape parameter will give no solution for a slope parameter with an extremely low (<0.6) DFR measurement.

In summary, parameters of the gamma distribution are related to drop concentration (intercept parameter), the proportionality of large and small drops (slope parameter), and the variance of drop size (shape parameter). The DFR is a function of the latter two physical quantities, but with only two reflectivity measurements, an additional constraint is needed on the gamma distribution to provide a solution for all three parameters. For global rainfall measurements, it is critical that these assumptions are physically realistic and accommodate the wide variety of DSDs observed in nature. In this study, we employ disdrometer measurements to develop constraints that are optimized for dual-frequency radar DSD retrieval algorithms.

3. Datasets and instrumentation

The DSD measurements used in this study were obtained at various NASA TRMM satellite validation sites and from field campaigns related to TRMM

TABLE 1. Precipitation regions and corresponding period and number of 1-min DSD observations for the disdrometer datasets used in this study. Some datasets were combined and others were split based on DSD characteristics. The regions will be referenced by the given abbreviations in subsequent tables and charts.

Region	Period	Obs	Mean R (mm h^{-1})	Mean d$BZ_{13.6}$
Central tropical Pacific (CTP)	May–Dec 2003–04	47 633	3.97	34.28
Florida Keys (FK)	Jul–Sep 2001–03	11 316	4.85	38.75
Amazon Basin of Brazil (westerly; BW)	Jan–Feb 1999	2885	3.53	37.56
Wallops Island, VA (tropical cyclones; WT)	2003–04	1840	4.50	34.49
Wallops Island (cellular convection) (WC)	2003–04	1620	14.67	45.51
Darwin, Australia (break) + Brazil (easterly; BE)	Jan–Mar 1994	923	5.08	39.33
	Jan–Feb 1999	759		
Darwin (monsoon; DM)	Jan–Mar 1994	5506	2.96	32.85
West Pacific (warm pool; TC)	Nov 1992–Feb 1993	8631	3.79	33.96
South China Sea (SCS)	Jul 1998	4251	5.29	37.39

(Table 1). These sites represent a variety of precipitation regimes, allowing examination of the sensitivity of our proposed dual-frequency radar DSD retrieval algorithm to regional variations in drop spectra. The datasets were classified into nine regions based on previous studies of DSD characteristics. The observations from two different islands of the Kwajalein atoll, located in the central tropical Pacific Ocean (CTP), contained similar DSD features. These islands are located near the intertropical convergence zone (Houze et al. 2004), and are thus representative of oceanic precipitation in the deep Tropics. Likewise, datasets from three consecutive summers showed nearly identical characteristics in deep convective rainfall in the Florida Keys (FK; Tokay et al. 2003a), and they were also merged. In contrast, the data from Brazil and Darwin, Australia, showed different characteristics depending on wind regime. The rainfall in the easterly wind regime in Brazil was found to be similar to rain during the break period in Darwin (Tokay et al. 2002); thus, these datasets are combined for our analysis (BE). However, the Brazil westerly regime (BW) and Darwin monsoon period (DM) DSDs were distinct and are treated separately in this study. Data from Wallops Island, Virginia (Tokay et al. 2005), were classified by storm type via examination of archive radar imagery. The resulting datasets represent precipitation from tropical cyclones (WT) and cellular convection (WC). We also include DSD measurements from the western tropical Pacific warm pool during the Tropical Ocean and Global Atmosphere Coupled Ocean–Atmosphere Experiment (TOGA COARE; Tokay and Short 1996) and the South China Sea Monsoon Experiment (SCSMEX) as stand-alone datasets. These final two regions are designated as TC and SCS, respectively.

Prior to deriving DSD parameters and bulk descriptors of rainfall from DSD observations, it is essential to be aware of the limitations of the instrument that was used to obtain them, in this study the Joss–Waldvogel disdrometer (JWD; Joss and Waldvogel (1967). The JWD is an impact-type disdrometer that transforms the vertical momentum of a raindrop impacting the 50 cm^2 sampling area into an electric pulse of which the amplitude is a function of the drop diameter. Drop diameters ranging from 0.3 to 5.3 mm are detected in 127 bins, which are aggregated by the disdrometer software into 20 bins so that a sufficient number of drops are present in each bin during a 1-min sampling period to represent the DSD at a wide range of rainfall intensities.

Like any other disdrometer, the JWD has shortcomings. These include dead time, which hinders the instrument's ability to detect more than one drop at a time, and background noise, which limits the detection of very small drops. The small disdrometer sampling area is a compromise between sampling a sufficient number of drops at low rainfall rates while minimizing the dead-time problem at high rainfall rates. The assumption of terminal fall speed is necessary to determine drop concentrations per unit volume from a surface-based measurement, but drop velocities can diverge from their theoretical terminal fall speed in stagnant air, resulting in under- or overestimates of drop diameter (Salles and Creutin 2003). Also, the impact method cannot distinguish the size of drops larger than 5.3 mm in diameter because of the insignificant increment in terminal fall speeds beyond this size.

These errors in the JWD measurements may lead to biases in derived quantities. For example, reflectivity is particularly sensitive to large-drop concentrations and the truncation at 5.3 mm could result in a negative reflectivity bias in heavy rainfall. To overcome these limitations, data from optical disdrometers (e.g., Hauser et al. 1984; Löffler-Mang and Joss 2000; Kruger and Krajewski 2002; Barthazy et al. 2004), which measure the size and velocity of hydrometeors, have been compared

with JWD measurements. Tokay et al. (2001) compared JWD-derived reflectivity, rain rate, and gamma parameters with the same quantities derived from video disdrometer (2DVD) measurements, which have the ability to measure drop sizes beyond 5.3 mm. The 2DVD also measured more small drops than the JWD in heavy rainfall as a result of the noise problem, but the impact on calculated rain rate was within 3%, and calculated reflectivities were within 1 dB. The ability of both JWD and 2DVD disdrometers to represent the reflectivity from the much larger sampling volume of radar profilers has been shown by Gage et al. (2000), who found good agreement between the two in stratiform rain.

Another significant issue is the sensitivity of derived gamma parameters to instrument errors. Tokay et al. (2001) showed that the gamma parameters derived from the average coincident spectra from both disdrometers were nearly identical, although subsets with fewer samples indicated a positive bias in the parameters derived from the 2DVD. While instruments such as the 2DVD promise to improve DSD measurements in the future, the current widespread deployment of the JWD in field experiments (Tokay et al. 2003b) makes it well suited to compare long-term records of DSD characteristics in different climate regimes.

The DSD, which is expressed in units of concentration per diameter interval in each bin (m^{-3} mm^{-1}), is derived by normalizing the raw disdrometer drop counts in each bin (C_i),

$$N_i = \frac{C_i}{\tau \alpha v_{t,i} \Delta D_i}, \tag{7}$$

where N_i is the drop concentration in the ith bin (m^{-3} mm^{-1}), τ is the time period (60 s) over which drops were counted, α is the disdrometer sampling area, $v_{t,i}$ is the terminal velocity of the midsize drop in the ith bin (m s^{-1}), following Beard (1976), and ΔD_i is the width of the ith bin (mm).

4. Analysis procedure

The goal of this study is to develop constraints on the three-parameter gamma distribution that results in the optimal retrieval of rain rate, liquid water content, and mean mass diameter from disdrometer-calculated dual-frequency radar measurements. To achieve this goal, we first address the potential sampling problems of the JWD, which can lead to biases in the parameters derived from the observations (Smith et al. 1993; Smith and Kliche 2005). To reduce errors related to undersampling, some form of averaging is usually performed on the disdrometer observations. Lee and Zawadzki (2005) have advocated compositing DSDs over reflectivity intervals, rather than averaging over time intervals or random samples, because reflectivity-based composites result in the most consistent Z–R relations when different regression techniques are used. However, it is possible that different rainfall physics may occur at a given reflectivity interval, and in these cases the average spectra cannot represent the underlying true variability. An analysis of the variability of the spectra in each reflectivity interval is given in appendix A and shows that there is generally more variability at reflectivities below 40 dB$Z_{13.6}$, where both convective and stratiform processes are common, and also in the continental regions. This variability should be taken into account when considering the parameters derived from the composite DSDs.

The composites were made for each region in 2-dB$Z_{13.6}$ intervals from 10 to 60 dB$Z_{13.6}$. This bin width resulted in sample sizes on the order of 100–1000 for most of the composite spectra. However, at the high end of this reflectivity range, fewer samples were available for inclusion in each composite, raising the question of whether or not these composites were truly representative of the region. Thus, a cutoff was established by examining the fitted gamma parameters for consistency from one reflectivity interval to the next. A minimum of 20 samples was found to be necessary under this criterion, corresponding to maximum reflectivities between 42 and 56 dB$Z_{13.6}$ for each region.

The ability of the composites to represent regional differences in DSD was evaluated by examining the spectra at each reflectivity interval. The composites from different datasets within the same climate region tended to form distinct clusters when compared with other regions, especially at reflectivities above 35 dB$Z_{13.6}$. This demonstrates that the differences between composites from different regions are significant relative to the differences within a region.

To develop constraints on the gamma distribution from these composites, the gamma parameters are fitted to each composite DSD using a method that incorporates the simulated dual-frequency radar measurements. The success of this or any other fitting algorithm depends on the degree to which the data resemble a gamma distribution. If there are significant deviations, such as multiple modes or inflection points, then some information will be lost in the fitted distribution. For applications to dual-frequency radar retrievals, the information contained in the DFR is primarily representative of the shape of the distribution at large drop sizes. This is because the reflectivities are approximately sixth-moment quantities and are thus heavily influenced by the concentration of larger drops. With these radar measurements, we desire to retrieve a DSD

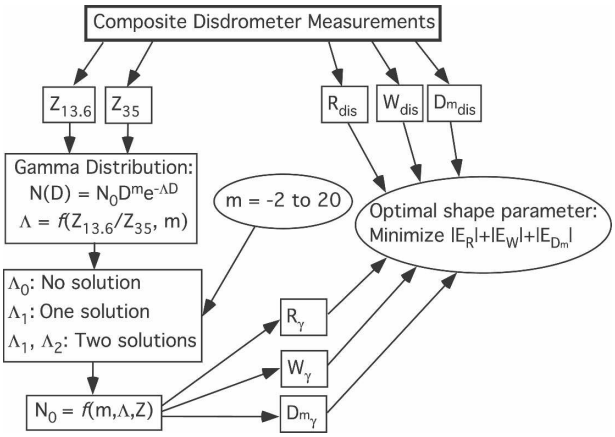

FIG. 3. Flowchart of the algorithm by which optimal shape parameter is determined.

that also accurately reproduces integral rainfall quantities, which are related to the third and fourth moments. Therefore, the gamma distributions we derive should reflect the shape of the distribution at larger drop sizes, even if this comes at the expense of accurately representing the concentration of small drops.

The fitting procedure (Fig. 3) begins with the calculation of reflectivity at 13.6 and 35 GHz from a discrete version of Eq. (2), where the numeric integration is performed from the minimum to maximum diameter. We also calculate integral rainfall quantities—rain rate R (mm h^{-1}), liquid water content W (g m^{-3}), and mean mass diameter D_m (mm)—for each composite DSD using Eqs. (8)–(10):

$$R = \frac{1 \times 10^{-6} \times 3600\pi}{6} \sum_{i=1}^{\eta} D_i^3 \upsilon_{t,i} N_i \Delta D_i, \tag{8}$$

$$W = \frac{1 \times 10^{-3} \rho_w \pi}{6} \sum_{i=1}^{\eta} D_i^3 N_i \Delta D_i, \quad \text{and} \tag{9}$$

$$D_m = \frac{\sum_{i=1}^{\eta} D_i^4 N_i \Delta D_i}{\sum_{i=1}^{\eta} D_i^3 N_i \Delta D_i}, \tag{10}$$

where η is the number of bins (20, for our datasets), σ_b is the backscattering cross section (mm^2) calculated for each frequency at a temperature of 20°C, D_i is the drop diameter (mm) at the middle of the ith bin, υ_t is the terminal velocity (m s^{-1}) as described in section 3, N_i is the drop concentration (m^{-3} mm^{-1}) defined in Eq. (7), and ρ_w is the density of liquid water (g cm^{-3}).

Next, we fit the slope and intercept parameters for a given shape parameter using the simulated dual-frequency reflectivity values. The slope parameter is calculated by numerically solving Eqs. (4) with the given shape parameter. This produces either one, two, or no solutions, depending on the DFR and value of the shape parameter imposed. The intercept parameter N_0 is then calculated by solving Eq. (3) for N_0 and substituting the previously obtained solutions for m and Λ:

$$N_0 = \frac{Z_e}{\sum_{i=1}^{\eta} \sigma_b(\lambda, D_i, T) D_i^m e^{-\Lambda D_i} \Delta D_i}, \tag{11}$$

where Z_e is either the 13.6- or 35-GHz reflectivity calculated from the disdrometer measurement. These derived gamma parameters correspond to a distribution that exactly reproduces both of the reflectivity measurements.

We derived these distributions for the same range of shape parameter used in Fig. 2, from −2 to 20, and incremented by 0.1. To complete the fitting process, the optimal shape parameter is selected by minimizing the sum of the absolute values of relative error E for rain rate, liquid water content, and mean mass diameter:

$$E = \frac{Q_{\text{retr}} - Q_{\text{obs}}}{Q_{\text{obs}}}, \tag{12}$$

where Q_{retr} and Q_{obs} are the gamma-retrieved and disdrometer-observed integral rainfall quantities, respectively. The magnitude of this error is lowest for the distribution that provides the closest estimate of that integral rainfall quantity. By summing the error magnitude from different integral rainfall quantities, we seek the gamma parameters that not only reproduce the DFR exactly, but also offer the best approximation of lower-moment integral rainfall quantities.

During the application of this fitting algorithm to the composite DSDs, two regimes were identified regarding the behavior of these errors and the corresponding optimal solution. At reflectivities less than 36–42 dB$Z_{13.6}$, depending on region, the DFR is less than 1, and thus two sets of solutions for slope parameter exist for a given shape parameter. This ambiguity is a direct result of the dual roots to Eq. (4). At higher reflectivities, the DFR is greater than 1, and thus only one solution exists. The DFR was sufficiently high in all cases to ensure the existence of one or two solutions.

For the dual-solution cases, the correct solution was determined by seeking the simultaneous minimization of integral rainfall quantity errors. This occurs for the second solution at reflectivities less than 22 dB$Z_{13.6}$ (Fig. 4a), and for the first solution at reflectivities greater than 28 dB$Z_{13.6}$ (Fig. 4e). The superiority of one

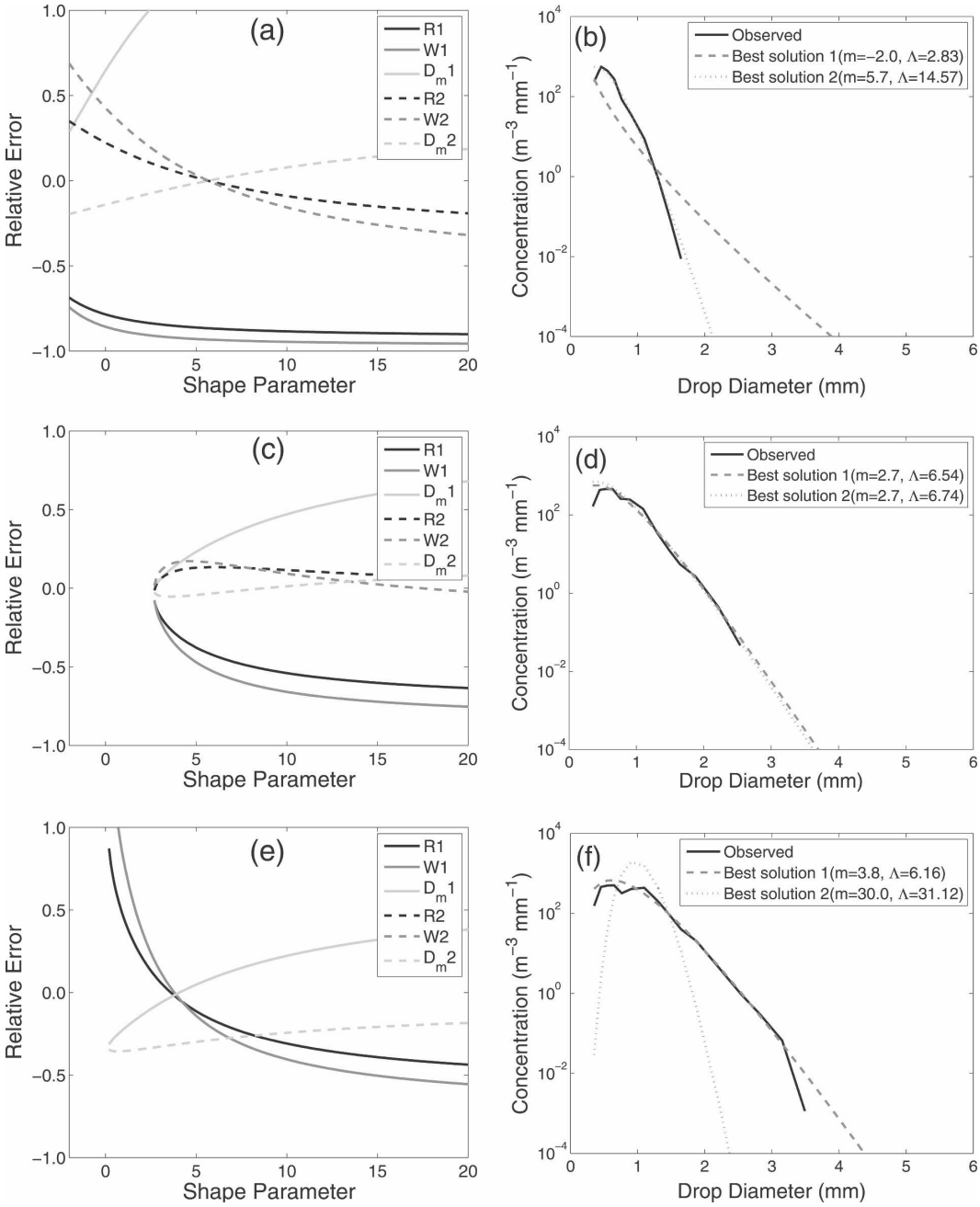

FIG. 4. Relative errors for the Kwajalein (a) 10–12-, (c) 20–22-, and (e) 30–32-dB$Z_{13.6}$ fitted vs observed DSDs as a function of shape parameter. (b), (d), (f) Best-fit gamma distributions from the first and second solutions for slope parameter are plotted for each of these DSDs, respectively.

solution over the other in these intervals is illustrated in Figs. 4b,f.

The reflectivity at which the optimal solution switched from second to first varied among different regions, but was always between 22 and 28 dB$Z_{13.6}$. For some composites in this intermediate range, second-solution error magnitudes for each integral rainfall quantity reached absolute minima at widely separated values of shape parameter (Fig. 4c). In these cases, relative error minima were also observed at the lowest shape parameter. Here, both the first and second solution fit the observed DSD well (Fig. 4d). This is not surprising because these solutions are close to one another in shape parameter–slope parameter space near

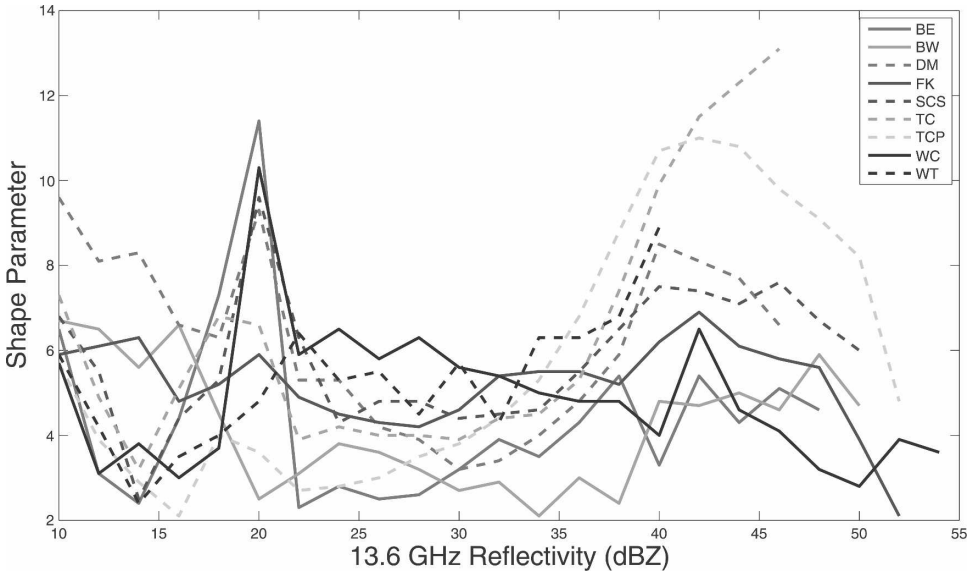

FIG. 5. Optimal shape parameter vs 13.6-GHz reflectivity for all datasets. Note the divergence of shape parameter from continental (solid) and oceanic (dashed) regions at reflectivities above 35 dB$Z_{13.6}$. The abbreviations for regions are given in Table 1.

the minimum shape parameter on a DFR curve (Fig. 2). Thus, this minimum shape parameter was considered optimal in these cases.

The curves in Figs. 4a,c,e also provide an indication of the errors that can be expected if a nonoptimal shape parameter is applied. Everywhere, except for a small range near the transition from the second to first solution for slope parameter, a lower-than-optimal shape parameter is associated with an overestimate of rain rate and liquid water content and an underestimate of mean mass diameter, and vice versa. Near the transition, however, these trends reverse. This can be explained by examining the DFR curves in Fig. 2. In the linear branches of these curves, D_m increases with shape parameter, but at the apex, D_m decreases with increasing shape parameter along the curve. The opposite sign of the D_m error with respect to rain rate and liquid water content errors is a result of the bias in dual-frequency retrievals toward higher moments of the DSD. For a lower-than-optimal value of shape parameter, the retrieved DSD will be flatter than the observed DSD. Thus, in order to reproduce the shape of the DSD at larger drop sizes, concentrations will be overestimated at the small drops, with the reverse being true for higher-than-optimal shape parameters.

5. Regional variability of optimal shape parameter

We obtained optimal shape parameters from the composite DSDs for all reflectivity intervals at each region. The behavior of the optimal shape parameter with respect to reflectivity and climate region reflects physical differences in the DSD among these regions. All regions showed a similar progression from the second to first solution with increasing reflectivity, but the values of the optimal shape parameter vary considerably between regions and between different reflectivity intervals within a region.

The optimal shape parameters at each reflectivity interval for all datasets, shown in Fig. 5 and appendix B, represent the different DSD characteristics in each region. Recall that the optimal shape parameter is more representative of the change in slope for mid- to large-sized drops than the curvature of the distribution immediately around the peak concentration at small drop sizes. Additionally, the slope parameter is calculated directly from the DFR and is also largely a measure of the exponential decay of the DSD at the large drops ($D > 3$ mm). Therefore, it is not surprising that the fitted gamma DSDs match observed DSDs very well at large-drop bins (Fig. 4). Although this fitting procedure can lead to significant concentration errors for the small-sized drops ($D < 1$ mm), particularly in DSDs with a wide range of drop sizes, these errors are of minimal importance to the quantities we seek to retrieve.

At the lowest reflectivity range we examined (10–20 dB$Z_{13.6}$), many regions exhibit a minimum shape parameter near 15 dB$Z_{13.6}$, indicating DSDs that are approaching exponential. The increase of shape parameter on either side of this minimum occurs for different

reasons on each side. On the low-reflectivity end the largest drop diameters are approximately 1.5 mm and the shape parameter represents the curvature of the concentration peak that occurs near 0.5 mm. On the high-reflectivity side of this minimum, the optimal shape parameter is more representative of the change in slope of medium-sized ($1 < D < 3$ mm) drop concentrations than the curvature around the peak.

At 22–35 dB$Z_{13.6}$, corresponding to both light and moderate rainfall, the optimal shape parameter is fairly steady at each region, but varies considerably from region to region. The steadiness of the shape parameter within each region, along with the increase of DFR with increasing 13.6-GHz reflectivity, indicates that the mean drop size increases with reflectivity in this range. The variability of the shape parameter between regions is a result of the differences in the shape of the DSD at drop sizes larger than 1.5 mm. The high shape parameters were associated with spectra that curve downward toward larger drop sizes, whereas the slopes of low shape parameter spectra were nearly constant at these drop sizes. Even though we did not explicitly separate convective and stratiform rainfall in our datasets, it is noteworthy that the higher shape parameters come from datasets that are dominated by convective rainfall (WT and WC).

At reflectivities above 35 dB$Z_{13.6}$ the results from oceanic and continental regions diverged, with shape parameters increasing for oceanic regions while remaining approximately constant for continental regions. The oceanic datasets reached a maximum shape parameter of 10–12 around the 40–45-dB$Z_{13.6}$ intervals before decreasing to 6–9 at 50 dB$Z_{13.6}$. This disparity in optimal shape parameter is caused by physical differences between continental and oceanic rainfall in deep convective precipitation and has been observed previously (Bringi et al. 2003). The higher value of the shape parameter in oceanic rainfall indicates a narrower distribution of drop sizes in oceanic rainfall relative to continental rainfall. At a given reflectivity, the oceanic spectrum has a smaller mean drop size than continental rainfall. This leads to significant differences in rain rate at a given reflectivity; for example, at 42 dB$Z_{13.6}$, rain rate varied from 9.9 mm h^{-1} in the Wallops convection dataset to 20.7 mm h^{-1} in the Darwin monsoon dataset.

6. Relationships between the shape and slope parameters

The variability of the shape parameter from region to region corresponds to significant variation in rain rates at a given reflectivity. This suggests that the use of a fixed shape parameter for dual-frequency rainfall retrievals will result in systematic regional biases. However, if the shape and slope parameters are correlated, then a relationship between the two, hereinafter denoted as an m–Λ relationship, may be employed during these retrievals to account for some of the observed variability. Such a relationship has been developed from disdrometer datasets by Zhang et al. (2001) and subsequently employed in dual-polarimetric radar-rainfall retrievals (Brandes et al. 2003) and radar data assimilation (Zhang et al. 2006). Although this relationship is supported by the work of Seifert (2005) via rain shaft model simulations, the video disdrometer datasets from which it was derived were limited to rainfall from Florida and Colorado, which is primarily continental in origin. Additionally, a minimum rain rate of 5 mm h^{-1} was imposed. Our data points that adhere to these criteria are in general agreement with the relationship of Zhang et al. (2001). However, the oceanic datasets have higher shape parameters and the light rainfall ($R < 5$ mm h^{-1}) DSDs have lower shape parameters than this relationship would suggest (Fig. 6a). These deviations are sufficiently significant to preclude a single m–Λ relationship from being used for all retrievals.

When only the m–Λ pairs from a particular dB$Z_{13.6}$ interval are considered (Fig. 6b), a strong linear relationship among the points from different regions emerges. For each reflectivity interval i, a least squares linear fit was made of the form

$$\Lambda = a_i m + b_i. \tag{13}$$

The coefficients a_i and b_i and the correlation coefficient are given for each reflectivity interval in appendix C. Positive values of a_i and b_i at all intervals indicate that at a given reflectivity, a higher shape parameter is associated with a higher slope parameter. This has the first-order effect of damping variations in D_m, but through combining Eqs. (5) and (13), it can be shown that D_m will increase with m if $4a < b$. Conversely, D_m decreases with m if $4a > b$. The first case is true for all reflectivity intervals below 36 dB$Z_{13.6}$, but above this level, the m–Λ relationships give a D_m that decreases with m. This is consistent with the higher rain rates we find in the regions with a high shape parameter at a given reflectivity.

The strength of each m–Λ relationship is given by the squared correlation coefficient, which averaged 0.934 for all reflectivity intervals. This coefficient was near 0.9 at low-reflectivity intervals, but greater than 0.97 at all intervals above 36 dB$Z_{13.6}$, indicating strong m–Λ relationships at high rainfall rates. This is significant because the greatest regional variation of shape parameter is found for these high rainfall rates, but an m–Λ relationship at the appropriate reflectivity interval ac-

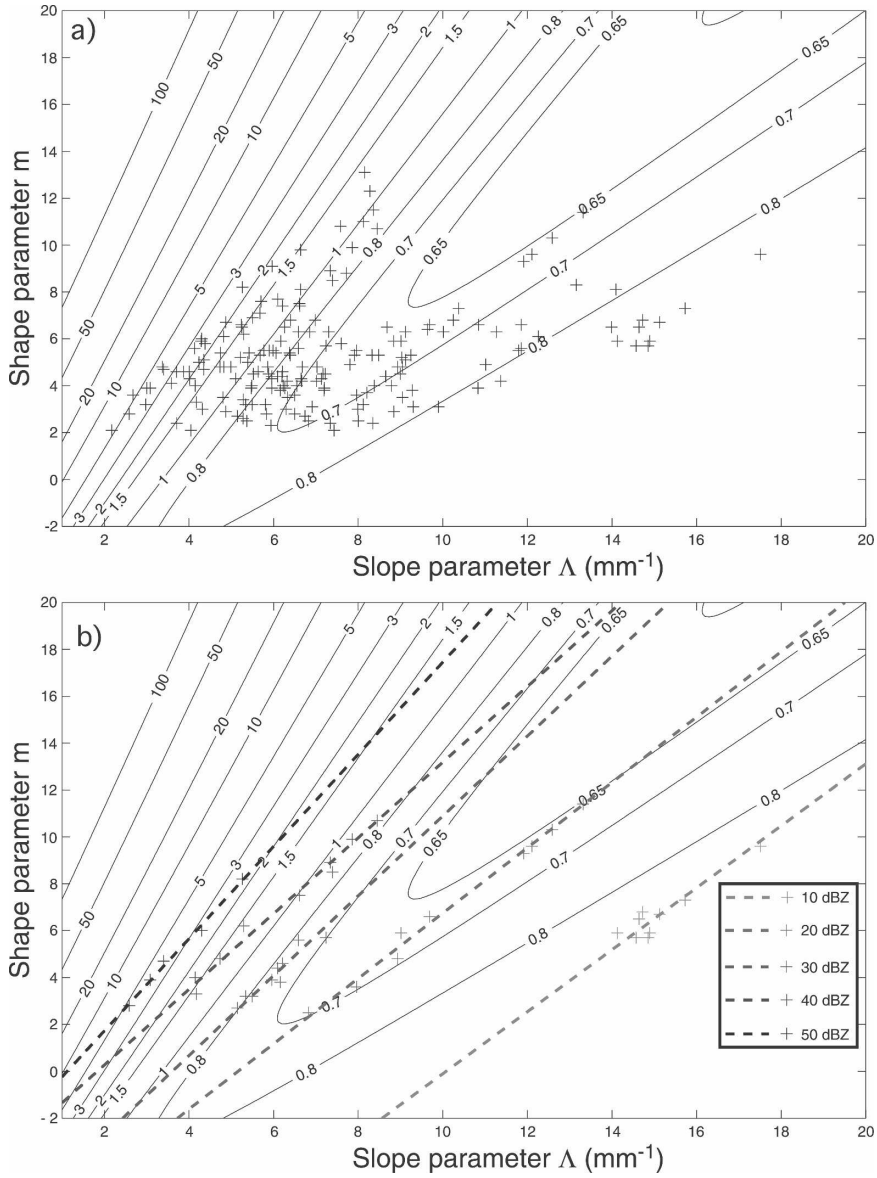

FIG. 6. (a) Scatterplot of (m–Λ) pairs for each reflectivity interval from all of our regions overlaid on the DFR contours from Fig. 2. (b) The (m–Λ) pairs from selected $\mathrm{dB}Z_{13.6}$ intervals along with their best-fit lines; (from left to right) linear fits are for the 10-, 20-, 30-, 40-, and 50-dBZ DSDs.

counts for this variation and could potentially result in more accurate DSD retrievals.

The parameters of the m–Λ relationships also evolve systematically with respect to reflectivity. The coefficients a_i and b_i both decrease with increasing 13.6-GHz reflectivity, which can be seen by the progression of the best-fit lines in Fig. 6b. As reflectivity increases this trend results in a smaller slope parameter for a given shape parameter, which is consistent with the presence of more large drops in high-reflectivity DSDs. This finding is also consistent with the results of Zhang et al. (2003), who determined that although statistical error in fitting methods can create m–Λ relationships, the coefficients represent a true relationship between DSD parameters. The following second-order polynomials fit the coefficients in Eq. (13) as functions of 13.6-GHz reflectivity Z:

$$a = 1.007 \times 10^{-4} Z^2 - 1.462 \times 10^{-2} Z + 0.989 \quad \text{and} \tag{14}$$

$$b = 3.827 \times 10^{-3} Z^2 - 4.007 \times 10^{-1} Z + 11.78. \tag{15}$$

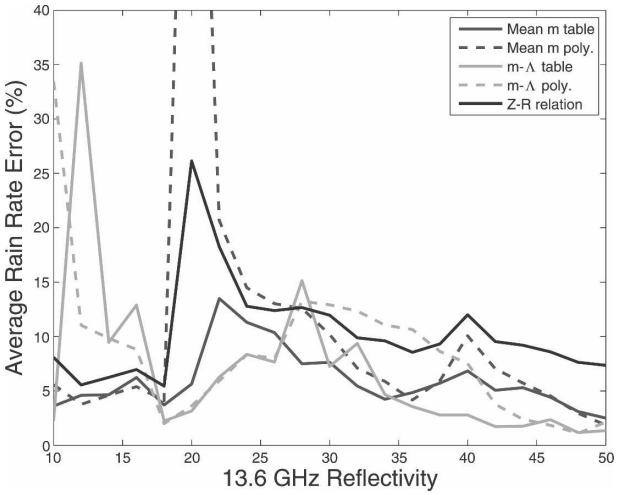

FIG. 7. Percent rain-rate error as a function of $dBZ_{13.6}$ for five retrieval methods. For the mean shape parameter and m–Λ relationship constraints, the tables are approximated by second-order polynomial relationships. An off-scale value of 89.4% in the polynomial Z–m relationship at 20 $dBZ_{13.6}$ is thought to be caused by the dual-solution ambiguity. Here, the first-solution threshold of 22 $dBZ_{13.6}$ results in the selection of the incorrect solution for some DSDs.

The correlation coefficients are 0.68 and 0.93 for Eqs. (14) and (15), respectively.

7. Evaluation of constraints

We compare two constraints on the gamma distribution for dual-frequency radar-rainfall retrieval. The first constraint is a fixed shape parameter and the second is a relationship between shape and slope parameters. The parameters of these constraints are allowed to vary with reflectivity. For the fixed shape parameter constraint, we use a mean shape parameter (see Table B1) to calculate rain-rate error E_i for each reflectivity interval at each site. The average magnitude of these errors is shown in Fig. 7. We also calculate the total error weighted by rain amount,

$$\text{Total Weighted Error} = \sum_{i=1}^{N_{\text{DSD}}} |E_i| w_i, \tag{16}$$

where N_{DSD} is the number of composites over which the weighted error is calculated, E_i is given by Eq. (12), and w_i is the contribution of rainfall in the ith reflectivity interval to total rainfall,

$$w_i = \frac{R_i n_i}{\sum_{j=1}^{N_{\text{DSD}}} R_j n_j}, \tag{17}$$

where n_i is the number of 1-min observations in the ith reflectivity interval. Likewise, we use m–Λ relationships (see Table C1) to calculate the same error statistics for this constraint. The weighted rain-rate error averaged over all regions for the fixed shape parameter constraint is 5.70%, as compared with 4.43% for the m–Λ relationships. At high reflectivities the strong correlation between shape and slope parameter contributes to lower errors for the m–Λ constraint than for the fixed shape parameter constraint (Fig. 7), which is reflected in the total weighted error.

An alternative to using the tables in the appendices is to apply polynomial relationships derived from them. The second-order polynomial fit for mean shape parameter as a function of $dBZ_{13.6}$ (Z) is

$$m = -4.64 \times 10^{-4} Z^2 + 3.91 \times 10^{-2} Z + 4.57. \tag{18}$$

The polynomial fits for the coefficients of the m–Λ relationships are given in Eqs. (14) and (15), respectively. These fitted polynomials are used in place of the tables to calculate the rain-rate error statistics. In terms of total weighted error, the polynomial relationships show some degradation of performance relative to that shown in the tables in the appendices, and the $Z_{13.6}$–m relationship outperforms the m–Λ relationship.

As a final basis for comparison, a $Z_{13.6}$–R relationship was derived from the datasets with a linear least squares fit to illustrate the advantage of dual- over single-frequency rainfall retrievals,

$$Z_{13.6} = 225 R^{1.54}. \tag{19}$$

The weighted error from the $Z_{13.6}$–R relation is 9.81%, about twice the amount resulting from the dual-frequency methods. Figure 7 indicates comparable performance of the single-wavelength $Z_{13.6}$–R relationship to the dual-frequency methods at low reflectivities (10–20 $dBZ_{13.6}$), but the dual-frequency methods outperform the $Z_{13.6}$–R relationship at medium and high reflectivities ($dBZ_{13.6} > 20$), resulting in the lower weighted errors for these methods.

The decreasing magnitude of the rain-rate error with increasing reflectivity is noted for both constraints. The advantage of the dual-frequency methods over the $Z_{13.6}$–R relation is also greatest at high reflectivities. These trends are a consequence of the additional information provided by the DFR, which is strongly related to the shape of the large-drop end of the spectrum. As reflectivity increases, these well-retrieved large drops increasingly contribute to the total rain rate and hence reduce the error magnitude. We also note that liquid water content errors (not shown) are greater in magni-

tude than rain-rate errors, a result of the stronger dependence of the former quantity on the poorly retrieved small-drop end of the spectrum.

The fixed shape parameter constraint results in regional biases that must be removed for applications such as long-term climate studies. A possible solution is to use different reflectivity–shape parameter relationships in different regions, but this requires definition of these regions, which cannot be done globally with our limited datasets. Furthermore, even in the same region, DSD characteristics may depend on wind regime (Tokay et al. 2002). In these situations, a fixed shape parameter would fail to capture this variability, possibly resulting in seasonal biases.

The m–Λ relationships show the potential to overcome the biases inherent in using a constraint of fixed shape parameter. These relationships are strongest at high reflectivities (dB$Z_{13.6} > 35$), where the regional biases of fixed shape parameter are most problematic. Another advantage of the m–Λ relationships is shown at 20–25 dB$Z_{13.6}$. Here, the two solutions for the fixed shape parameter constraint are given by the double intersection of a DFR contour. The m–Λ relationships we derived only intersect each contour once, eliminating this ambiguity. However, there are two reasons why an m–Λ relationship might fail to provide accurate solutions. A low correlation coefficient could give solutions far from the optimal values. This occurs at 25–35 and 10–15 dB$Z_{13.6}$, where even a single-frequency $Z_{13.6}$–R relation outperforms the m–Λ constraint. Another problem is that even a highly correlated fit could fail if it is nearly parallel to the DFR contours. This is because only a small change in DFR, which might result from an error in attenuation correction, could lead to a large change in the retrieved DSD.

8. Summary and conclusions

The retrieval of a three-parameter gamma distribution representing DSD from dual-frequency radar measurements requires an a priori constraint. In this study, we have employed disdrometer observations from distinct climatic regimes to develop constraints that are representative of the wide regional variation in drop spectra. We derived two constraints—a fixed shape parameter and the shape parameter–slope parameter relationship. The shape parameter–slope parameter relationships provide a slight advantage over the fixed shape parameter terms of overall rain amount–weighted rain-rate error, and both dual-frequency methods are approximately twice as accurate as the $Z_{13.6}$–R relationship. However, each constraint has strengths and weaknesses; the m–Λ relationships generally perform better than the fixed shape parameter at high reflectivities, and vice versa at low reflectivities. The regional DSD differences in shape parameter were found to be most significant both in magnitude and in the context of lower internal DSD variability (appendix A) at high reflectivities (>40 dB$Z_{13.6}$), which coincides with the strongest m–Λ relationships, so it is at these high reflectivities that our results are most significant and applicable.

The performance of these constraints with polarimetric radars or at different frequencies than those used here should be similar to our results in principle because DFR at different frequencies and the polarimetric differential reflectivity Z_{DR} are both also weighted toward the sixth moment of the DSD, and thus the retrieved parameters will result in optimal rainfall estimation. However, the slopes of the DFR curves may be different than those shown in Fig. 2, and certain properties of our relationships, such as the elimination of dual solutions near 20 dB$Z_{13.6}$, may not be applicable at other frequencies. The angle at which the DFR or Z_{DR} curves intersect the m–Λ relationships also determines the susceptibility of DSD retrieval to measurement error, which may thus be different for other frequencies/polarizations than in this study.

The constraints that have been developed in this study may be incorporated into DSD profile retrieval algorithms that are being considered for the dual-frequency radar on the GPM core satellite. However, while these constraints appear to be valid for DSDs from a wide variety of climate regimes, they need to be verified against independent DSD observations from other regions. For validation of our constraints above the ground, profiler observations of the vertical structure of DSDs in precipitation systems could be analyzed.

Regarding applications to GPM, it is important to note that dual-frequency retrievals will be limited by the sensitivity of the radar receiver. The 13.6-GHz radar will only be sensitive to reflectivities higher than about 17 dB, whereas at 35 GHz, the minimum sensitivity will be 12 dB, according to recent design specifications (Iguchi et al. 2003). The latter will allow GPM to estimate rainfall that is currently undetectable by the TRMM PR, which may contribute to disagreements between the PR and TMI (Berg et al. 2006), but these retrievals will be done at a single frequency. In heavy rainfall, attenuation will limit the range of 35-GHz measurements, and in extreme cases the same may occur at 13.6 GHz. In these situations, DSD estimates at range gates where both frequencies are available could be used to formulate optimal $Z_{13.66}$–R relations at subsequent attenuated range gates.

In this study, we have investigated only one component of satellite-based dual-frequency radar-rainfall retrieval algorithms. The effects of ice and snow, bright-band interaction, and attenuation from atmospheric water vapor, cloud water, and hydrometeors are not considered herein. Despite these additional challenges, our results show considerable promise for the ability of dual-frequency radar measurements, augmented by optimal constraints, to accurately measure DSD.

Acknowledgments. The authors thank Robert Meneghini of NASA Goddard Space Flight Center for thoughtful comments and suggestions during the course of research for this study. David Marks of NASA Goddard Space Flight Center also provided helpful comments prior to submission. The first author also thanks Johannes Verlinde, Eugene Clothiaux, and Jerry Harrington of The Pennsylvania State University for their role as reviewers of this material prior to its presentation as a thesis. This work was supported by the 2004 NASA Summer Institute for Atmospheric, Biospheric, and Hydrospheric Sciences under Per Gloersen, NSF Grant ATM-0127360, an AMS graduate fellowship sponsored by NASA's Earth Science Enterprise, and NASA's TRMM program through NAG5-13615 under Ramesh Kakar, Program Scientist.

APPENDIX A

Variability within DSD Composites

In section 4 we aggregate DSDs by an observable quantity (13.6-GHz reflectivity) with the implicit assumption that DSD variability within a reflectivity interval is primarily the result of random noise, which we seek to minimize through averaging. However, this variability may also be the result of different rain physics at a given reflectivity, which is retained in the larger sampling volume of a radar. Therefore, the derived parameters may not be representative of all rain at a given reflectivity. This issue could be particularly problematic at low and intermediate reflectivities where precipitation may be stratiform or convective in origin.

In this appendix, we briefly present some additional statistics to characterize the variability within the composites. One measure of this variability is the standard deviation of drop concentration in each bin measured by the JWD. However, drop concentrations vary over many orders of magnitude and are not normally distributed because of the nonexistence of negative values. A closely related measure of variability that is less sensitive to extremes in the data is the spread between the first and third quartile.

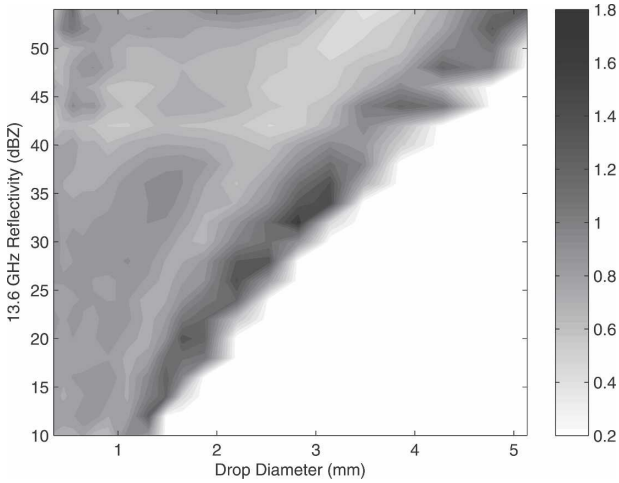

FIG. A1. Normalized spread of drop concentration in each disdrometer size bin, averaged over all regions at each reflectivity interval.

This spread was computed for each bin of each composite DSD and normalized by the concentration in each bin. The mean normalized concentration in each drop size bin and reflectivity interval is shown in Fig. A1. In each reflectivity interval, maxima are noted at the largest drop-containing bins, with minima adjacent to the left. This behavior is consistent with a set of spectra containing members that have different proportions of large and small drops, but are constrained within a narrow reflectivity range. The result is that drop concentrations pivot around the point of minimum spread. The degree to which this pivot occurs is an indication of the variability of the DSDs within a reflectivity interval.

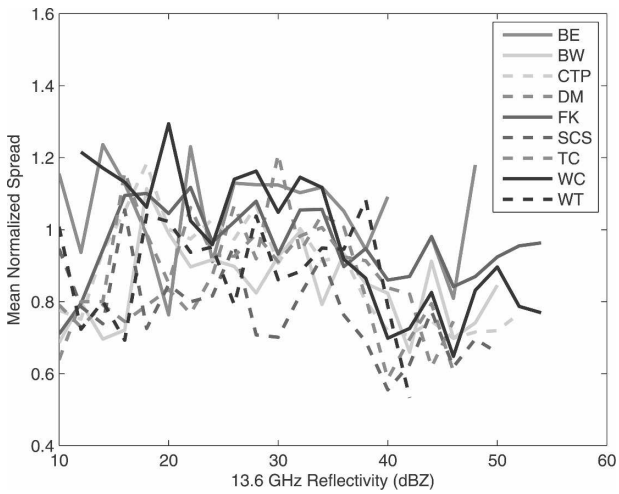

FIG. A2. Mean normalized spread of drop concentration for each region by reflectivity.

Another notable trend in Fig. A1 is the decrease in spread that occurs at reflectivities higher than 40 dB$Z_{13.6}$. This probably represents the point at which rainfall transitions from a mixture of stratiform and convective processes to being exclusively convective, thereby reducing the variability of DSDs caused by different rain physics. This trend is also illustrated in Fig. A2, where we note a decrease in normalized spread at all regions near 40 dB$Z_{13.6}$. Figure A2 also shows the relative variability contrasted by region; for example, WC and FK tend to have higher normalized spreads than SCS and DM.

APPENDIX B

Optimal Shape Parameter Statistics

The derivation of optimal shape parameter is outlined in section 4. The resulting summary statistics of mean, standard deviation, and extremes were calculated at each reflectivity interval for all available regions and are given in Table B1. A polynomial fit for the mean as a function of 13.6-GHz reflectivity is given in Eq. (18). Note that above 40–42 dB$Z_{13.6}$, some regions did not have composite DSDs because of insufficient samples. Therefore, the statistics for the high-reflectivity intervals are for a subset of all regions. The following list gives the maximum reflectivity interval at each site: TCP (52–54), WT (40–42), WC (54–56), FK (52–54), BW (50–52), BE (48–50), DM (46–48), TC (46–48), and SCS (50–52).

TABLE B1. Statistics of optimal shape parameter for each reflectivity interval. The abbreviations are given in Table 1.

dB$Z_{13.6}$ interval	Mean	Std dev	Max (region)	Min (region)
10–12	6.7	1.2	9.6 (DM)	5.7 (WC, TCP)
12–14	5.0	1.7	8.1 (DM)	3.1 (WC, BE)
14–16	4.2	2.1	8.3 (DM)	2.4 (WT, BE)
16–18	4.5	1.5	6.6 (DM, BW)	2.1 (TCP)
18–20	5.2	1.3	7.3 (BE)	3.7 (WC)
20–22	7.1	3.2	11.4 (BE)	2.5 (BW)
22–24	4.5	1.6	6.4 (WT)	2.3 (BE)
24–26	4.4	1.2	6.5 (WC)	2.8 (TCP, BE)
26–28	4.2	1.1	5.8 (WC)	2.5 (BE)
28–30	4.1	1.1	6.3 (WC)	2.6 (BE)
30–32	4.1	1.1	5.7 (WT)	2.7 (BW)
32–34	4.3	0.8	5.4 (WC, FK)	2.9 (BW)
34–36	4.5	1.2	6.3 (WT)	2.1 (BW)
36–38	5.1	1.1	6.8 (TCP)	3.0 (BW)
38–40	5.9	1.8	8.8 (TCP)	2.4 (BW)
40–42	7.1	2.7	10.7 (TCP)	3.3 (BE)
42–44	7.7	2.4	11.5 (TC)	4.7 (BW)
44–46	7.2	2.9	12.3 (TC)	4.3 (BE)
46–48	7.1	3.0	13.1 (TC)	4.1 (WC)
48–50	5.9	2.0	9.1 (TCP)	3.2 (WC)
50–52	5.1	2.1	8.2 (TCP)	2.8 (WC)
52–54	3.6	1.4	4.8 (TCP)	2.1 (FK)

APPENDIX C

Shape Parameter–Slope Parameter Relationships

At each reflectivity interval, a linear least squares relationship [Eq. (13)] was derived between the optimal shape parameter and corresponding slope parameter of each available composite DSD. Table C1 gives the coefficients of these linear relationships and the squared correlation coefficient r^2 at each reflectivity interval. Note that the number of contributing data points decreased from 9 to 8 at 42–44 dB$Z_{13.6}$, and then to 6 at 48–50 dB$Z_{13.6}$, 5 at 50–52 dB$Z_{13.6}$, and 3 at 52–54 dB$Z_{13.6}$. Polynomial relationships between the linear coefficients and 13.6-GHz reflectivity are given in Eqs. (14) and (15).

TABLE C1. Coefficients of linear shape parameter–slope parameter relationship with correlation coefficients at each reflectivity interval.

dB$Z_{13.6}$ interval	a	b	r^2
10–12	0.757	10.077	0.877
12–14	0.930	6.925	0.898
14–16	0.928	5.723	0.936
16–18	0.833	5.432	0.849
18–20	0.590	6.164	0.957
20–22	0.717	5.160	0.991
22–24	0.767	4.358	0.964
24–26	0.716	4.183	0.895
26–28	0.660	3.970	0.906
28–30	0.535	4.183	0.796
30–32	0.587	3.607	0.904
32–34	0.535	3.492	0.833
34–36	0.641	2.663	0.912
36–38	0.696	2.107	0.911
38–40	0.638	2.047	0.974
40–42	0.619	1.833	0.983
42–44	0.603	1.508	0.988
44–46	0.556	1.563	0.992
46–48	0.507	1.649	0.988
48–50	0.511	1.334	0.996
50–52	0.509	1.123	0.993
52–54	0.446	1.244	0.999

REFERENCES

Barthazy, E., S. Göke, R. Schefold, and D. Högl, 2004: An optical array instrument for shape and fall velocity measurements of hydrometeors. *J. Atmos. Oceanic Technol.,* **21,** 1400–1416.

Battan, L. J., 1973: *Radar Observation of the Atmosphere*. University of Chicago Press, 324 pp.

Beard, K. V., 1976: Terminal velocity and shape of cloud and precipitation drops aloft. *J. Atmos. Sci.,* **33,** 851–864.

Berg, W., T. L'Ecuyer, and C. Kummerow, 2006: Rainfall climate regimes: The relationship of regional TRMM rainfall biases to the environment. *J. Appl. Meteor. Climatol.,* **45,** 434–454.

Brandes, E. A., G. Zhang, and J. Vivekanandan, 2003: An evaluation of a drop distribution–based polarimetric radar rainfall estimator. *J. Appl. Meteor.,* **42,** 652–660.

Bringi, V. N., G.-J. Huang, V. Chandrasekar, and E. Gorgucci, 2002: A methodology for estimating the parameters of a gamma raindrop size distribution model from polarimetric radar data: Application to a squall-line event from the TRMM/Brazil campaign. *J. Atmos. Oceanic Technol.,* **19,** 633–645.

——, V. Chandrasekhar, J. Hubbert, E. Gorgucci, W. L. Randeu, and M. Schoenhuber, 2003: Raindrop size distribution in different climatic regimes from disdrometer and dual-polarized radar analysis. *J. Atmos. Sci.,* **60,** 354–365.

Eccles, P. J., and E. A. Mueller, 1971: X-band attenuation and liquid water content estimation by a dual-wavelength radar. *J. Appl. Meteor.,* **10,** 1252–1259.

Gage, K. S., C. R. Williams, P. E. Johnston, W. L. Ecklund, R. Cifelli, A. Tokay, and D. A. Carter, 2000: Doppler radar profilers as calibration tools for scanning radars. *J. Appl. Meteor.,* **39,** 2209–2222.

Goldhirsh, J., and I. Katz, 1974: Estimation of raindrop size distribution using multiple wavelength radar systems. *Radio Sci.,* **9,** 439–446.

Haddad, Z. S., S. L. Durden, and E. Im, 1996: Parameterizing the raindrop size distribution. *J. Appl. Meteor.,* **35,** 3–13.

——, J. P. Meagher, S. L. Durden, E. A. Smith, and E. Im, 2006: Drop size ambiguities in the retrieval of precipitation profiles from dual-frequency radar measurements. *J. Atmos. Sci.,* **63,** 204–217.

Hauser, D., P. Amayenc, B. Nutten, and P. Waldteufel, 1984: A new optical instrument for simultaneous measurement of raindrop diameter and fall speed distributions. *J. Atmos. Oceanic Technol.,* **1,** 256–269.

Houze, R. A., Jr., S. Brodzick, C. Schumacher, S. E. Yuter, and C. R. Williams, 2004: Uncertainties in oceanic radar rain maps at Kwajalein and implications for satellite validation. *J. Appl. Meteor.,* **43,** 1114–1132.

Iguchi, T., 2005: Possible algorithms for the Dual-frequency Precipitation Radar (DPR) on the GPM core satellite. Preprints, *32nd Conf. on Radar Meteorology,* Albuquerque, NM, Amer. Meteor. Soc. 5R.4. [Available online at http://ams.confex.com/ams/pdfpapers/96470.pdf.]

——, H. Hanado, N. Takahashi, S. Kobayashi, and S. Satoh, 2003: The dual-frequency precipitation radar for the GPM core satellite. *IEEE Trans. Geosci. Remote Sens.,* **46,** 1698–1700.

Joss, J., and A. Waldvogel, 1967: A spectrograph for the automatic analysis of raindrops. *Pure Appl. Geophys.,* **68,** 240–246.

Kruger, A., and W. F. Krajewski, 2002: Two-dimensional video disdrometer: A description. *J. Atmos. Oceanic Technol.,* **19,** 602–617.

Kummerow, C., W. Barnes, T. Kozu, J. Shiue, and J. Simpson, 1998: The Tropical Rainfall Measuring Mission (TRMM) sensor package. *J. Atmos. Oceanic Technol.,* **15,** 809–817.

Kuo, K.-S., E. A. Smith, Z. Haddad, E. Im, T. Iguchi, and A. Mugnai, 2004: Mathematical–physical framework for retrieval of rain DSD properties from dual-frequency Ku–Ka-band satellite radar. *J. Atmos. Sci.,* **61,** 2349–2369.

Lee, G., and I. Zawadzki, 2005: Variability of drop size distributions: Noise and noise filtering in disdrometric data. *J. Appl. Meteor.,* **44,** 634–652.

Liao, L., and R. Meneghini, 2005: A study of air/space-borne dual-wavelength radar for estimation of rain profiles. *Adv. Atmos. Sci.,* **22,** 841–851.

Löffler-Mang, M., and J. Joss, 2000: An optical disdrometer for measuring size and velocity of hydrometeors. *J. Atmos. Oceanic Technol.,* **17,** 130–139.

Mardiana, R., T. Iguchi, and N. Takahashi, 2004: A dual-frequency rain profiling method without the use of a surface reference technique. *IEEE Trans. Geosci. Remote Sens.,* **42,** 2214–2225.

Marshall, J. S., and W. M. Palmer, 1948: The distribution of raindrops with size. *J. Meteor.,* **5,** 165–166.

Meagher, J. P., and Z. S. Haddad, 2006: To what extent can raindrop size be determined by a multiple-frequency radar? *J. Appl. Meteor. Climatol.,* **45,** 529–536.

Meneghini, R., T. Kozu, H. Kumagai, and W. C. Boncyk, 1992: A study of rain estimation methods from space using dual-wavelength radar measurements at near-nadir incidence over ocean. *J. Atmos. Oceanic Technol.,* **9,** 364–382.

——, H. Kumagai, J. Wang, T. Iguchi, and T. Kozu, 1997: Microphysical retrievals over stratiform rain using measurements from an airborne dual-wavelength radar-radiometer. *IEEE Trans. Geosci. Remote Sens.,* **35,** 487–506.

Rincon, R. F., and R. H. Lang, 2002: Microwave link dual-wavelength measurements of path-average attenuation for the estimation of drop size distribution and rainfall. *IEEE Trans. Geosci. Remote Sens.,* **40,** 760–770.

Salles, C., and J.-D. Creutin, 2003: Instrumental uncertainties in *Z–R* relationships and raindrop fall velocities. *J. Appl. Meteor.,* **42,** 279–290.

Seifert, A., 2005: On the shape–slope relation of drop size distributions in convective rain. *J. Appl. Meteor.,* **44,** 1146–1151.

Smith, P. L., and D. V. Kliche, 2005: The bias in moment estimators for parameters of drop size distribution functions: Sampling from exponential distributions. *J. Appl. Meteor.,* **44,** 1195–1205.

——, Z. Liu, and J. Joss, 1993: A study of sampling-variability effects in raindrop size observations. *J. Appl. Meteor.,* **32,** 1259–1269.

Tokay, A., and D. A. Short, 1996: Evidence from tropical raindrop spectra of the origin of rain from stratiform versus convective clouds. *J. Appl. Meteor.,* **35,** 355–371.

——, A. Kruger, and W. F. Krajewski, 2001: Comparison of drop size distribution measurements by impact and optical disdrometers. *J. Appl. Meteor.,* **40,** 2083–2097.

——, ——, ——, P. A. Kucera, and A. J. P. Filho, 2002: Measurements of drop size distribution in the southwestern Amazon region. *J. Geophys. Res.,* **107,** 8052, doi:10.1029/2001JD000355.

——, D. B. Wolff, K. R. Wolff, and P. Bashor, 2003a: Rain gauge and disdrometer measurements during the Keys Area Microphysics Project (KAMP). *J. Atmos. Oceanic Technol.,* **20,** 1460–1477.

——, K. R. Wolff, P. Bashor, and O. K. Dursun, 2003b: On the measurement errors of the Joss-Waldvogel disdrometer. Preprints, *31st Int. Conf. on Radar Meteorology,* Seattle, WA,

Amer. Meteor. Soc., P3A.2. [Available online at http://ams.confex.com/ams/pdfpapers/64350.pdf.]

——, P. G. Bashor, and K. R. Wolff, 2005: Error characteristics of rainfall measurements by collocated Joss–Waldvogel disdrometers. *J. Atmos. Oceanic Technol.,* **22,** 513–527.

Ulbrich, C. W., 1983: Natural variations in the analytical form of the raindrop size distribution. *J. Climate Appl. Meteor.,* **22,** 1764–1775.

——, and D. Atlas, 1998: Rainfall microphysics and radar properties: Analysis methods for drop size spectra. *J. Appl. Meteor.,* **37,** 912–923.

Williams, C. R., 2002: Simultaneous ambient air motion and raindrop size distributions retrieved from UHF vertical incident profiler observations. *Radio Sci.,* **37,** 1024, doi:10.1029/2000RS002603.

Zhang, G., J. Vivekanandan, and E. A. Brandes, 2001: A method for estimating rain rate and drop size distribution from polarimetric radar measurements. *IEEE Trans. Geosci. Remote Sens.,* **39,** 830–841.

——, ——, ——, R. Meneghini, and T. Kozu, 2003: The shape–slope relation in observed gamma raindrop size distributions: Statistical error or useful information? *J. Atmos. Oceanic Technol.,* **20,** 1106–1119.

——, J. Sun, and E. A. Brandes, 2006: Improving parameterization of rain microphysics with disdrometer and radar observations. *J. Atmos. Sci.,* **63,** 1273–1290.